#### **CONFERENCE PRE-PRINT**

# SIMULATIONS OF RMP CONFIGURATIONS FOR TUNGSTEN IMPURITY CONTROL IN EAST TOKAMAK

Z.H. GAO, S.Y.DAI, Z.X.WEN, D.Z. WANG

Key Laboratory of Materials Modification by Laser, Ion and Electron Beams (Ministry of Education), School of Physics, Dalian University of Technology

Dalian, China

Email: daishuyu@dlut.edu.cn

H.M. ZHANG

Hefei Institutes of Physical Science, Chinese Academy of Sciences Hefei, China

G.Z. HAO Southwestern Institute of Physics Chengdu, China

Y. FENG Max-Planck-Institute für Plasmaphysik Greifswald, Germany

# Abstract

High-Z tungsten (W) accumulation in EAST degrades plasma performance and threatens steady-state operation. This work examines optimization of resonant magnetic perturbation (RMP) phasing—specifically the upper/lower coil phase difference  $\Delta \varphi$ —to mitigate W sputtering and accumulation, using MARS-F for plasma-response field analysis coupled to EMC3-EIRENE impurity transport simulations. Three principal results are obtained. First, the impurity-suppression phase inferred from vacuum fields peaks at  $\Delta \varphi = 0^\circ$ , whereas inclusion of plasma response shifts the effective phase owing to screening and amplification; MARS-F indicates that shielding reshapes the resonant edge topology, explaining mismatches when relying on vacuum predictions alone. Second, complete W-suppression windows appear only with plasma response for n=1, spanning  $\Delta \varphi \approx 0^\circ - 135^\circ$ . The mechanism is resonant amplification of edge perturbations that enhances boundary stochasticity, increases recycling, and lowers target temperatures, reducing incident ion energy below W sputtering thresholds. Third, the  $\Delta \varphi$  range that suppresses edge-localized modes in EAST overlaps with the window for W reduction, suggesting that established ELM-suppression criteria based on the total field at the last rational surface can serve as proxies for impurity-control efficacy. These findings provide actionable guidance for RMP phasing to minimize tungsten sources and accumulation on EAST.

# 1. INTRODUCTION

Tungsten (W) has been adopted as a leading plasma-facing material in present and next-step tokamaks due to its high melting point, low steady-state sputtering yield under hydrogen isotopes, and excellent thermo-mechanical properties [1–3]. The deployment of W divertors in tokamak such as ASDEX Upgrade and EAST, and the planned use in ITER, aim to withstand extreme heat and particle fluxes at the plasma boundary [4–6]. A persistent concern is that W impurities can be generated by physical and chemical sputtering from divertor targets and first-wall elements, then migrate into confined plasmas. Even trace concentrations of high-Z W produce strong line and continuum radiation that cools the plasma, deteriorates confinement, and under unfavorable conditions can contribute to discharge termination [7–10]. Understanding and controlling the generation, transport, and radiation of W in the edge and scrape-off layer (SOL) is therefore essential for reliable long-pulse operation.

Resonant magnetic perturbations (RMPs) provide a well-established tool for modifying the edge transport and magnetic topology, historically applied for edge-localized mode (ELM) control [11–13]. By introducing three-dimensional helical fields, RMPs reshape field-line connection patterns, alter cross-field transport, and affect neutral recycling and impurity sources at divertor surfaces. Their impact on impurity behavior depends sensitively on the phase of the applied perturbation [14–16]. Recent studies indicate that RMPs may either mitigate impurity accumulation by enhancing edge transport. However, a systematic assessment of how RMP toroidal phase jointly regulate tungsten sources, spatial distribution, and radiation in the edge remains incomplete.

This study addresses that gap using a targeted, fully three-dimensional edge modeling workflow. The applied perturbation fields are first computed with the MARS-F code for both vacuum and plasma-response cases at different coil phases, then superimposed on the equilibrium magnetic field. The perturbed magnetic topology, together with boundary conditions, is provided to the EMC3-EIRENE code to simulate the edge plasma and W impurity transport, including surface sputtering and prompt re-deposition. By scanning the RMP toroidal phase and contrasting vacuum and plasma-response fields, the modeling quantifies changes in tungsten source strength, SOL and divertor distributions, thereby identifying operational windows in which W amount is minimized and impurity penetration is reduced. The results provide physics guidance for optimizing RMP phasing as an impurity control actuator in tokamak edge plasmas.

The remainder of the paper is organized as follows. Section 2 introduces the two computational tools employed in this study, MARS-F for constructing vacuum and plasma-response perturbation fields, and EMC3-EIRENE for three-dimensional edge plasma and impurity transport simulations. Section 3 analyzes how the applied RMPs modify the boundary magnetic topology. Section 4 investigates the resulting impacts on tungsten sputtering and transport. Section 5 provides a summary of the main findings.

# 2. SIMULATION MODEL

#### 2.1. MARS-F code

RMPs reshape the edge magnetic topology and can drive it toward a partially stochastic state. In modeling, two field representations are typically employed. Vacuum fields are constructed by superposing the equilibrium field (without RMP) and the perturbation generated solely by the external coils, neglecting any plasma-induced currents. Plasma-response fields augment the vacuum fields with the additional perturbations arising from currents induced within the plasma by the applied RMP. The latter are computed with MARS-F, which solves the linearized, singlefluid resistive MHD equations in toroidal geometry to obtain the self-consistent plasma response.

MARS-F code solves the following single fluid, full MHD, resistive plasma equations:

$$i(\Omega_{\rm RMP} + n\Omega)\vec{\xi} = \vec{v} + (\vec{\xi} \cdot \nabla \Omega)R\vec{\Phi} \tag{1}$$

$$i\rho(\Omega_{_{RMP}}+n\Omega)\vec{v}=-\nabla p+\vec{j}\times\vec{B}+\vec{J}\times\vec{b}-\rho[2\Omega\vec{Z}\times\vec{v}+(\vec{v}\cdot\nabla\Omega)R\vec{\Phi}]-\rho\kappa_{_{\parallel}}\left|k_{_{\parallel}}v_{_{th,i}}\right|[\vec{v}+(\vec{\xi}\cdot\nabla)\vec{V}_{_{0}}]_{_{\parallel}} \eqno(2)$$

$$i(\Omega_{RMP} + n\Omega)\vec{b} = \nabla \times (\vec{v} \times \vec{B}) + (\vec{b} \cdot \nabla\Omega)R\vec{\Phi} - \nabla \times (\eta\vec{j})$$

$$i(\Omega_{RMP} + n\Omega)p = -\vec{v} \cdot \nabla P - \Gamma P \nabla \cdot \vec{v}$$
(4)

$$i(\Omega_{RMP} + n\Omega)p = -\vec{v} \cdot \nabla P - \Gamma P \nabla \cdot \vec{v}$$
(4)

$$\vec{i} = \nabla \times \vec{b} \tag{5}$$

where R is the major radius of the plasma,  $\vec{\Phi}$  is the unit vector along the toroidal angle  $\Phi$  of the torus, and  $\vec{Z}$  is the unit vector in the direction perpendicular to the toroidal plane. n is the toroidal mode number. The plasma resistivity is denoted by  $\eta$ . The variables  $\vec{\xi}$ ,  $\vec{v}$ ,  $\vec{b}$ ,  $\vec{j}$ , and p represent the plasma displacement, perturbed velocity, magnetic field, current, and pressure, respectively. The equilibrium magnetic field, current, and pressure are denoted by  $\vec{B}$ ,  $\vec{J}$ , and P.

In this work, the plasma resistivity profile  $\eta$  is prescribed analytically using a Spitzer model, i.e.,  $\eta \propto T_e^{(-3/2)}$ evaluated from the equilibrium electron-temperature profile. The plasma boundary is held fixed. The computational domain is constructed by extending the last closed flux surface (LCFS) radially to an artificial outer boundary at  $\rho = 4$  ( $\rho$  is the normalized minor-radius coordinate with  $\rho = 1$  at the LCFS). At this boundary we impose a perfectly conducting-wall condition by setting the normal component of the perturbed magnetic field to zero (n $\delta B = 0$ ). The RMP coils lie inside the computational boundary, so the coil-current perturbations are included and superposed on the axisymmetric equilibrium field (and, when specified, further combined with the MARS-F plasma response). The parallel sound wave damping coefficient  $\kappa_{\parallel}$ , which determines the damping intensity, is set to  $\kappa_{\parallel} = 1.5$ .

#### 2.2. EMC3-EIRENE code

The 3D Monte Carlo edge transport code, EMC3-EIRENE, calculates plasma parameters in the edge region by solving the steady-state conservation equations for mass, momentum, and energy:

$$\nabla \cdot (\mathbf{n}_{i} \mathbf{u}_{i \parallel} \vec{\mathbf{e}}_{\parallel} - \mathbf{D}_{\perp} \ddot{\mathbf{I}}_{\perp} \cdot \nabla \mathbf{n}_{i}) = \mathbf{S}_{p}$$

$$\tag{6}$$

$$\nabla \cdot \vec{\mathbf{e}}_{\parallel}(\mathbf{m}_{i}\mathbf{n}_{i}\mathbf{u}_{i\parallel}^{2} - \eta \vec{\mathbf{e}}_{\parallel} \cdot \nabla \mathbf{u}_{i\parallel}) - \nabla \cdot \vec{\mathbf{I}}_{\perp} \cdot \mathbf{D}_{\perp} \nabla (\mathbf{m}_{i}\mathbf{n}_{i}\mathbf{u}_{i\parallel}) = -\vec{\mathbf{e}}_{\parallel} \cdot \nabla \mathbf{p} + \mathbf{S}_{m}$$

$$\tag{7}$$

$$\nabla \cdot \vec{\mathbf{e}}_{\parallel}(\frac{5}{2}T_{e}n_{i}u_{i\parallel} - \kappa_{e}\vec{\mathbf{e}}_{\parallel} \cdot \nabla T_{e}) - \nabla \cdot \vec{\mathbf{I}}_{\perp} \cdot (\chi_{e}n_{i}\nabla T_{e} + \frac{5}{2}T_{e}D_{\perp}\nabla n_{i}) = -\frac{3m_{e}}{m_{i}}\frac{n_{e}}{\tau_{ei}}(T_{e} - T_{i}) + S_{ee} - S_{e,cool}$$
(8)

$$\nabla \cdot \vec{e}_{\parallel}(\frac{5}{2}T_{i}n_{i}u_{i\parallel} - \kappa_{i}\vec{e}_{\parallel} \cdot \nabla T_{i}) - \nabla \cdot \vec{I}_{\perp} \cdot (\chi_{i}n_{i}\nabla T_{i} + \frac{5}{2}T_{i}D_{\perp}\nabla n_{i}) = -\frac{3m_{e}}{m_{i}}\frac{n_{e}}{\tau_{ei}}(T_{e} - T_{i}) + S_{ei}$$
 (9)

where  $D_{\perp}$ ,  $\chi_e$  and  $\chi_i$  are particle perpendicular transport coefficient, electron and ion energy perpendicular transport coefficient. The impurity transport module is incorporated within EMC3-EIRENE, allowing for the feedback of impurity radiation to the plasma for self-consistent iteration, ultimately resulting in a converged steady-state solution [44]. The impurity continuity and momentum equations can be expressed as follows:

$$\begin{split} \nabla_{\parallel} \cdot \left( n_{z} V_{z_{\parallel}} \right) - \nabla_{\perp} \cdot \left( D_{imp} \nabla_{\perp} n_{z} \right) &= S_{z} \\ - \frac{1}{n_{z}} \frac{dp_{z}}{ds} + Z_{imp} e E_{\parallel} + m_{z} \frac{V_{\parallel} - V_{z_{\parallel}}}{\tau_{s}} + 0.71 Z_{imp}^{2} \frac{dT_{e}}{ds} + \beta_{i} Z_{imp}^{2} \frac{dT_{i}}{ds} &= 0, \\ \beta_{i} &= 3 \frac{\mu + 5 \sqrt{2} Z_{imp}^{2} (1.1 \mu^{5/2} - 0.35 \mu^{3/2}) - 1}{2.6 - 2 \mu + 5.4 \mu^{2}}, \\ \mu &= \frac{m_{z}}{m_{z} + m_{i}} \end{split}$$
(11)

The subscripts i and Z denote the plasma ions and impurity species, respectively, with mi and  $m_Z$  representing their corresponding masses.  $Z_{imp}$  represents the impurity charge states and  $S_Z$  denotes the impurity source term. Impurity transport parallel to the magnetic field lines is mainly determined by the parallel velocity, which is predominantly governed by friction force and ion thermal gradient force along the parallel direction. Perpendicular transport is controlled by the impurity perpendicular transport coefficient  $D_{imp}$ .

# 3. RESULTS

# 3.1. Simulation setup

The simulation parameters are based on the discharge #67578 on EAST. This H-mode discharge is characterized by a plasma current of  $I_p$  = 450 kA, a normalized beta  $\beta_N$  = 0.67, and a double-null configuration. In this shot, the magnetic axis is located at a major radius of  $R_a$  = 1.91 m and the toroidal magnetic field has a strength of  $B_t$  = 2.48 T. The safety factor at the axis is  $q_0$  = 2.1, while at the separatrix it is  $q_a$  = 11.3. The RMP coil system on EAST consists of two groups, each containing 8 coils. These coils are symmetrically arranged both above and below the midplane. The current in each coil is determined by the toroidal angle  $\phi_k$  at the geometric center of the coil, and the current amplitude follows  $I_k$  =  $A\cos(n\phi_k - \phi_0)$ . In this discharge, the current amplitude is A = 8.8 kAt, toroidal mode number is n = 1. Figure 1 shows poloidal and toroidal positions of the RMP coils on EAST, respectively.

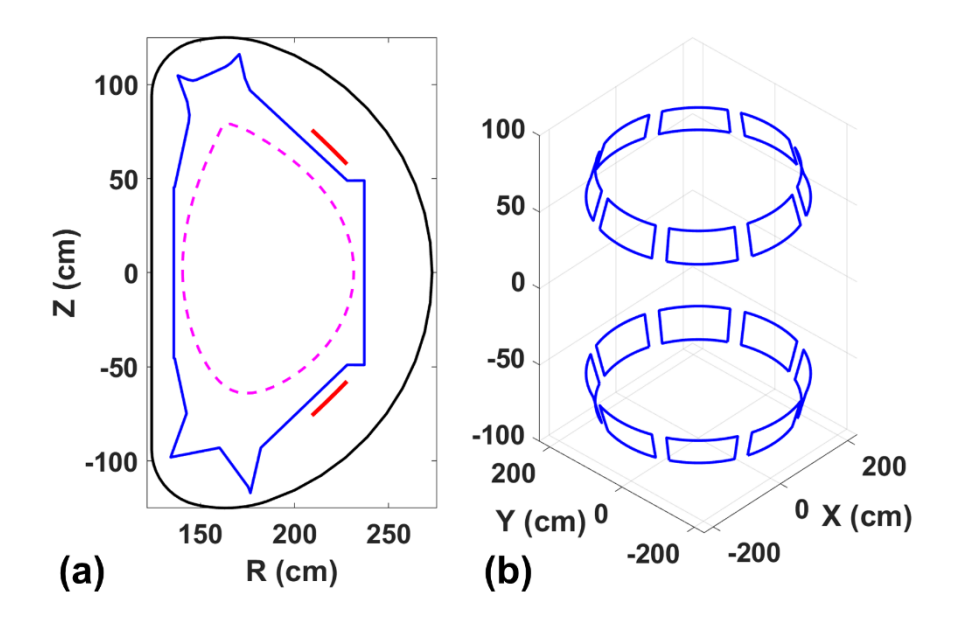


FIG. 1. (a) Poloidal and (b) toroidal position of RMP coils on EAST.

The reference equilibrium has a relatively low normalized beta, with the key radial profiles (density, temperature, safety factor, etc.) shown in Figure 2. Because the toroidal rotation profile on EAST is not tightly constrained, a sensitivity study was conducted to assess its influence on tungsten radiation. Test simulations spanning the expected range of rotation velocities indicate that rotation has a negligible effect on the modeled W radiative power under the conditions considered. For simplicity and consistency, a common toroidal-rotation profile is therefore adopted throughout this study. The reference plasma remains below the Troyon no-wall  $\beta_N$  limit for the onset of the ideal external kink instability.

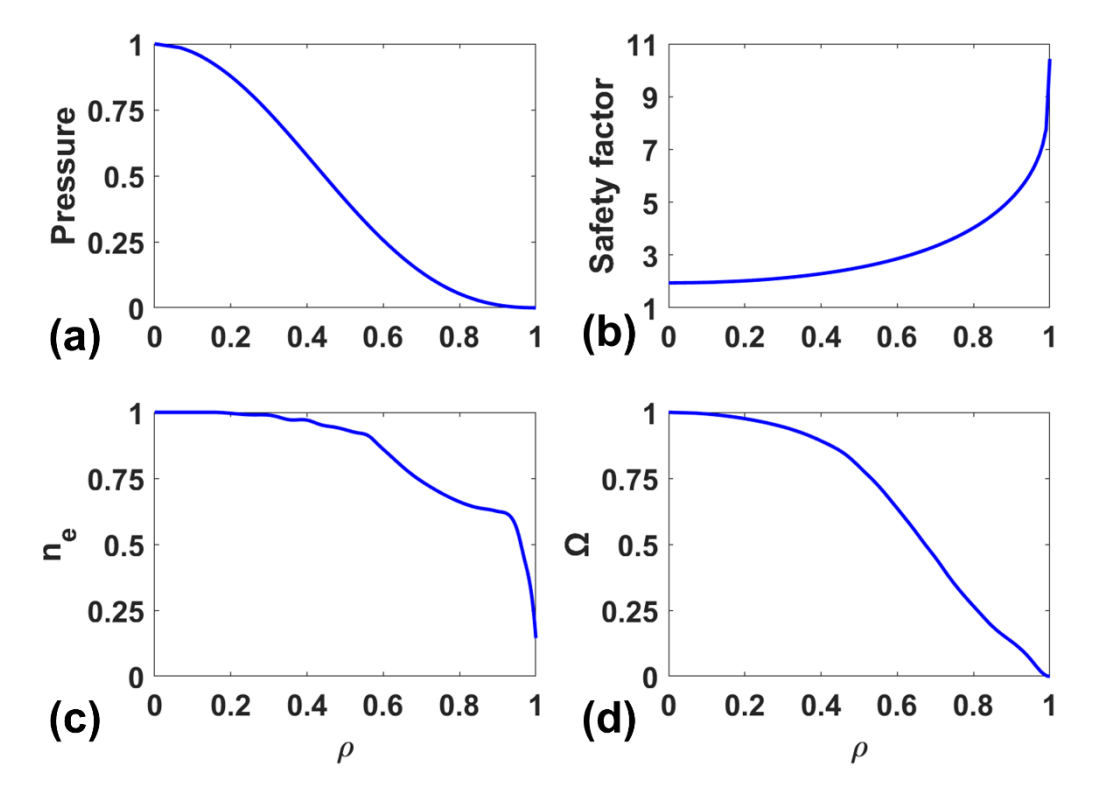


FIG. 2. Radial profiles of (a) the normalized plasma pressure, (b) the safety factor, (c) the plasma density normalized to unit on the magnetic axis and (d) the normalized plasma toroidal rotation frequency for the chosen reference equilibrium on EAST.

# 3.2. Plasma response versus coil phasing

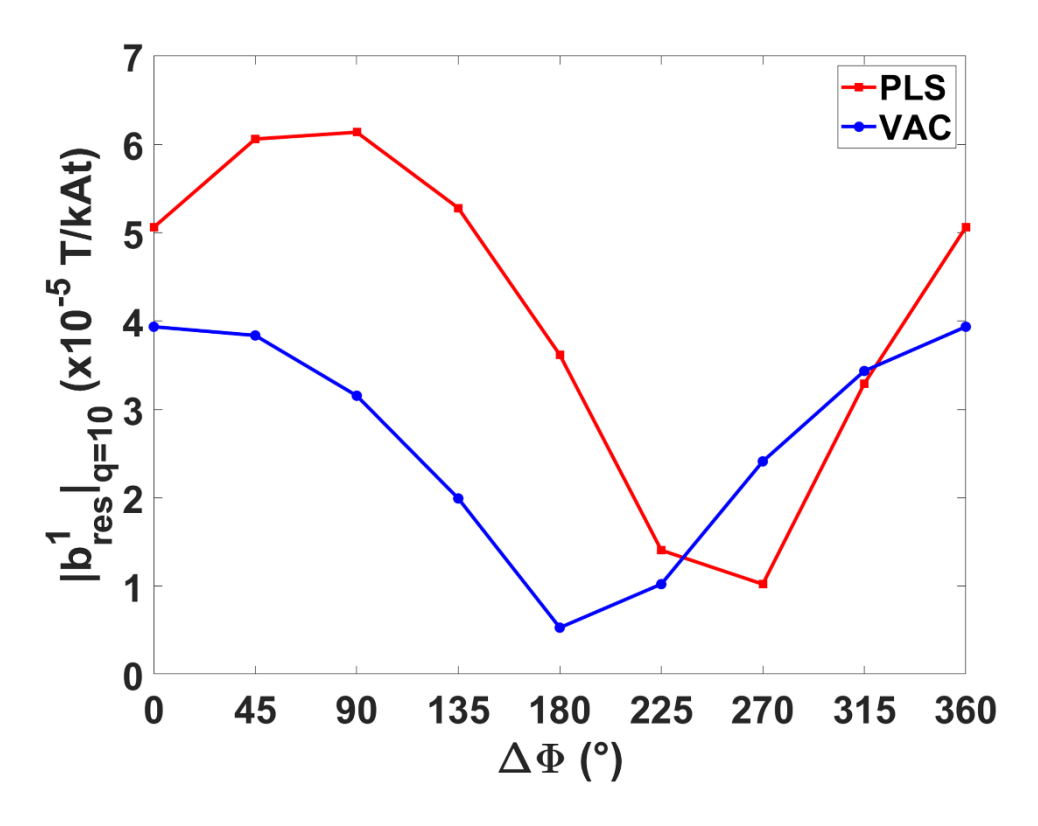


FIG. 3. Phase scan of the resonant normal field amplitude  $|b_{res}|$  at the q=10 rational surface as a function of the upper/lower coil phase difference  $\Delta\Phi$  for n=1 RMPs, from MARS-F calculations. Red squares (PLS) denote the plasmaresponse field and blue circles (VAC) denote the vacuum field; values are normalized to coil current.

Figure 3 presents a phase scan of the resonant normal field amplitude  $|b_{res}|^1$  at the q=10 rational surface versus the upper/lower coil phase difference  $\Delta\Phi$ , normalized by coil current, comparing plasma-response calculations (PLS; red squares) with vacuum-field calculations (VAC; blue circles). Across most phases the PLS amplitude exceeds the VAC value and peaks for  $\Delta\Phi\approx45^\circ-90^\circ$  at  ${\sim}6\times10^{-5}$  T/kAt, whereas VAC remains  ${\sim}3-4\times10^{-5}$  T/kAt. The VAC minimum appears near  $\Delta\Phi\approx180^\circ$  ( ${\sim}0.5\times10^{-5}$ ), while the PLS minimum is shifted to  $\Delta\Phi\approx270^\circ$  ( ${\sim}0.7-1.0\times10^{-5}$ ), revealing an  ${\sim}90^\circ$  offset of the extrema between vacuum and plasma-response fields; the two curves approach each other around  $\Delta\Phi\approx315^\circ$  and return to levels comparable to those at  $\Delta\Phi=0^\circ$  by  $360^\circ$ . These trends indicate that plasma response both amplifies the edge resonant field and displaces the optimal/suppressed phasing, implying that vacuum-only predictions would misidentify the effective impurity-control window.

#### 3.3. Effect on target erosion

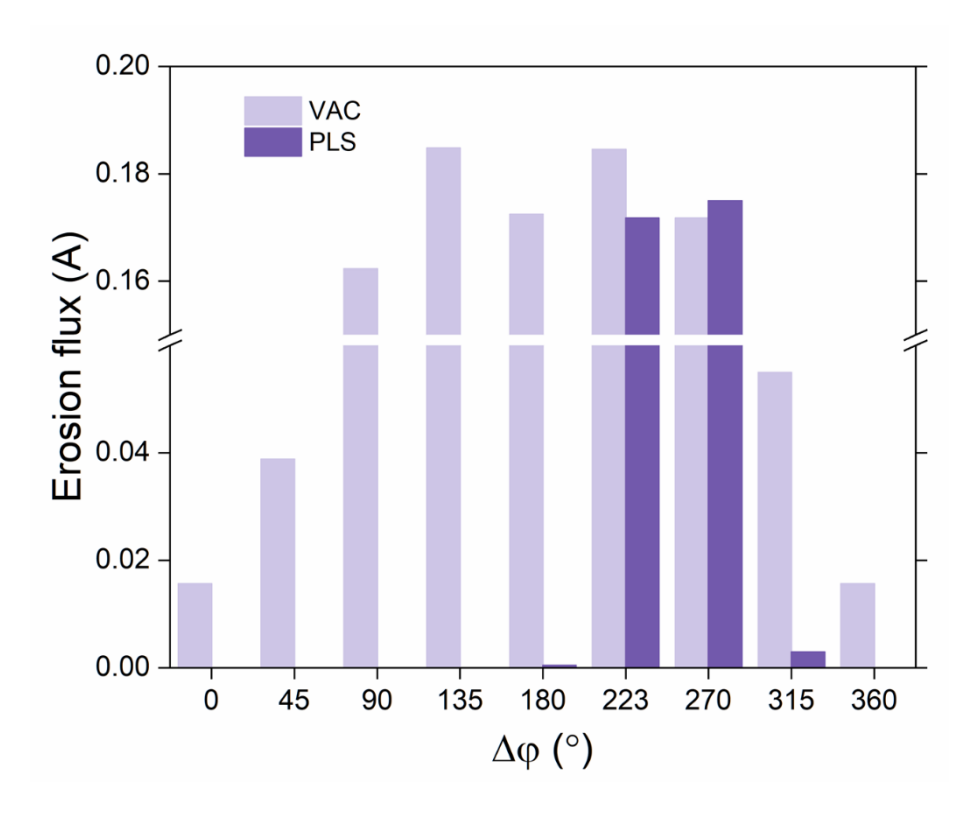


FIG. 4. Phase dependence of tungsten erosion flux  $\Gamma_{ero}$  under n=1 RMPs as a function of the upper/lower coil phase difference  $\Delta \varphi$ . Light bars (VAC) denote vacuum-field calculations and dark bars (PLS) denote plasma-response calculations from EMC3–EIRENE coupled with MARS-F fields. The ordinate shows erosion flux in A; a y-axis break is used to resolve both near-zero and peak values.

Figure 4 presents the phase scan of the divertor tungsten erosion flux predicted by EMC3-EIRENE for vacuum and plasma-response fields. In the vacuum case,  $\Gamma$  is substantial across  $\Delta \phi = 0^{\circ}\text{-}180^{\circ}$ , with a broad maximum around  $\Delta \phi \approx 90^{\circ}\text{-}135^{\circ}$  ( $\approx 0.16\text{-}0.19$  A) and still elevated values near  $\Delta \phi = 180^{\circ}$ . In contrast, the plasma-response calculation yields negligible erosion throughout  $\Delta \phi \lesssim 180^{\circ}$ , indicating an extended suppression window, and finite erosion appears only for larger phase differences, rising sharply near  $\Delta \phi \approx 223^{\circ}$  –  $270^{\circ}$  (peaking  $\approx 0.17$  A) and then decreasing toward  $\Delta \phi \approx 315^{\circ}\text{-}360^{\circ}$ . The phase selectivity and overall reduction of  $\Gamma$  in the plasma-response case are consistent with RMP-induced modifications of edge magnetic topology and transport that cool the target region and lower the incident ion energy below the tungsten sputtering threshold over  $\Delta \phi \lesssim 135^{\circ}\text{-}180^{\circ}$ , whereas the vacuum field lacks this self-consistent screening and retains strong erosion near the resonance-enhanced phases.

#### 3.4. Effect on impurity amount

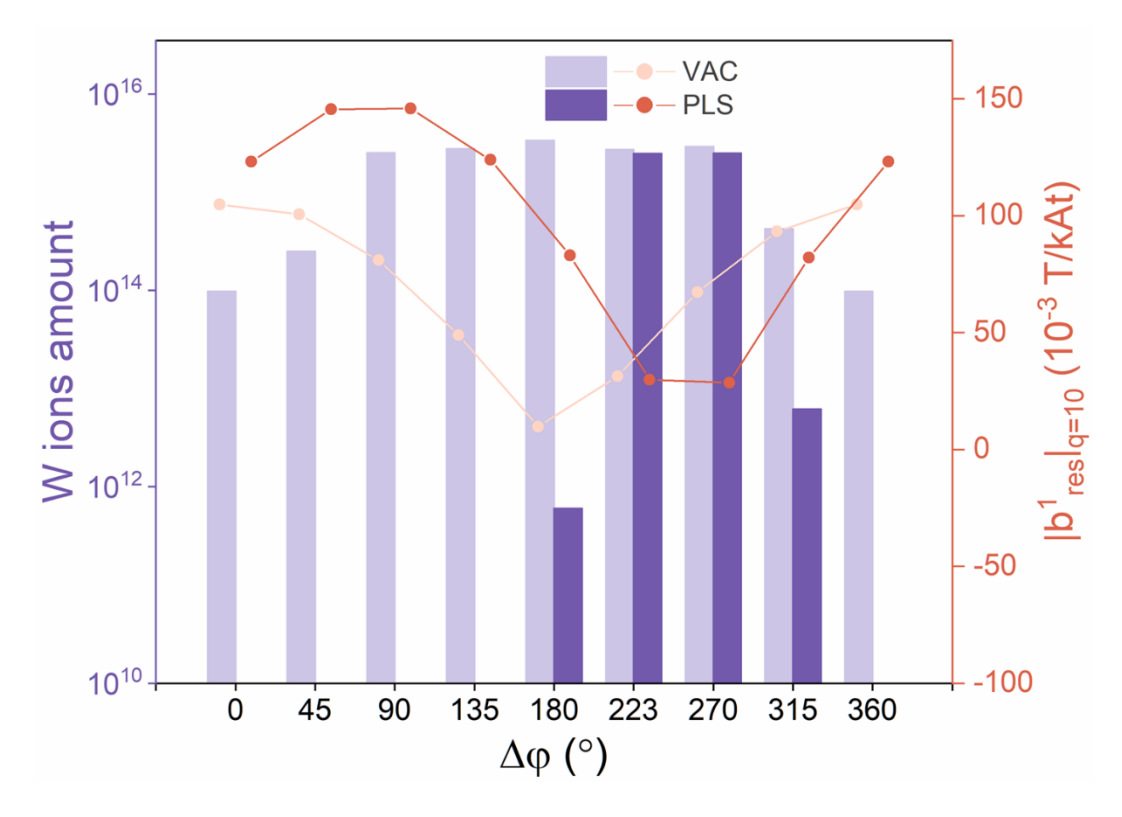


FIG. 5. Phase dependence of tungsten ion inventory (bars, left log axis) and resonant normal field  $|b_{res}|$  at q = 10 (red curve, right axis) versus upper/lower coil phase difference  $\Delta \varphi$  for n = 1 RMPs. Light bars: vacuum field (VAC); dark bars: plasma response (PLS).

Figure 5 presents a joint phase scan of impurity content and resonant field strength obtained with EMC3–EIRENE coupled to MARS-F. The bars (left, logarithmic scale) show the total number of W ions in the edge/SOL; the overlaid red curve (right axis, units  $10^{-3}$  T/kAt) gives  $|b_{res}|^1$  at the q=10 surface. When plasma response is included (PLS), an extended impurity-suppression window appears for  $\Delta\phi \lesssim 180^\circ$ , during which the W inventory is reduced by orders of magnitude relative to the vacuum calculation (VAC). In the PLS case, tungsten reappears only for larger phases, rising around  $\Delta\phi \approx 223^\circ-315^\circ$  as the resonant field weakens, consistent with reduced edge stochasticity and higher target temperatures that lift the incident ion energy above the sputtering threshold. By contrast, the vacuum field retains substantial W over  $\Delta\phi = 0^\circ-180^\circ$  and does not exhibit a complete suppression window. Importantly, the low-W phasing under PLS aligns with the ELM-suppression window previously identified on EAST when using the total (vacuum + response) field at the last rational surface, indicating a shared operational window in which the same RMP phasing simultaneously minimizes tungsten sources/accumulation and suppresses ELM activity.

# 4. SUMMARY

This work optimizes RMP phasing for tungsten control on EAST by coupling MARS-F (vacuum and plasma-response fields) with EMC3–EIRENE (3D edge plasma and impurity transport). Phase scans of the upper/lower coil difference  $\Delta \phi$  for n = 1 show that inclusion of plasma response both amplifies the resonant normal field at the edge and shifts its extrema by ~90° relative to the vacuum prediction. As a result, a robust impurity-suppression window appears only with plasma response ( $\Delta \phi \approx 0^{\circ}$  – 135°, extending toward ~180° depending on parameters), during which divertor W erosion is strongly reduced and the modeled W inventory in the edge/SOL drops by orders of magnitude. The mechanism is consistent with resonantly enhanced edge stochasticity and modified connection lengths that increase recycling and cool the target, lowering incident ion energy below the W sputtering threshold; for larger phases ( $\Delta \phi \approx 223^{\circ}$  – 315°) the resonant field weakens and W reappears. Importantly, the low-W phasing coincides with the ELM-suppression window derived from the total (vacuum + response) field at the last rational surface, indicating a shared operational window and enabling established ELM metrics to serve as practical proxies for impurity-control optimization. These results explain the mismatch

#### IAEA-CN-316/INDICO 2893 TH-D

encountered when relying on vacuum fields alone and highlight plasma-response-aware phase control as an effective route to minimize tungsten sources and accumulation on EAST.

#### **ACKNOWLEDGEMENTS**

This work was supported by National MCF Energy R&D Program of China No: 2024YFE03000200, National Natural Science Foundation of China under Grant Nos. 12475213 and 12235002.

# REFERENCES

- [1] Bucalossi J, Missirlian M, Moreau P et al, The WEST project: Testing ITER divertor high heat flux component technology in a steady state tokamak environment, Fusion Engineering and Design **89** (2014) 907-12
- [2] Bourdelle C, Artaud J F, Basiuk V et al, WEST Physics Basis, Nuclear Fusion 55 (2015) 063017
- [3] Richou M, Missirlian M, Guilhem D et al, Design and preliminary thermal validation of the WEST actively cooled upper divertor, Fusion Engineering and Design **98-99** (2015) 1394-1398
- [4] Romanelli F, Overview of the JET results with the ITER-like wall, Nuclear Fusion 53 (2013) 104002
- [5] Matthews G F, Plasma operation with an all metal first-wall: Comparison of an ITER-like wall with a carbon wall in JET, Journal of Nuclear Materials **438** (2013) S2-S10
- [6] Neu R, Dux R, Kallenbach A et al, Tungsten: an option for divertor and main chamber plasma facing components in future fusion devices, Nuclear Fusion 45 (2005) 209-218
- [7] Dux R, Bobkov V, Herrmann A et al, Plasma-wall interaction and plasma behaviour in the non-boronised all tungsten ASDEX Upgrade, Journal of Nuclear Materials **390-391** (2009) 858-863
- [8] Neu R, Bobkov V, Dux R et al, Ten years of W programme in ASDEX Upgrade—challenges and conclusions, Physica Scripta **T138** (2009) 014038
- [9] Wan B N, Liang Y F, Gong X Z et al, Overview of EAST experiments on the development of high-performance steadystate scenario, Nuclear Fusion **57** (2017) 102019
- [10] Pitts R A, Carpentier S, Escourbiac F et al, A full tungsten divertor for ITER: Physics issues and design status, Journal of Nuclear Materials 438 (2013) S48-S56
- [11] Doerner R P, Baldwin M J, De Temmerman G et al, Codeposition of deuterium with ITER materials, Nuclear Fusion **49** (2009) 035002
- [12] Pütterich T, Neu R, Dux R et al, Calculation and experimental test of the cooling factor of tungsten, Nuclear Fusion **50** (2010) 025012
- [13] Loarte A, Koechl F, Leyland M J et al, Evolution of plasma parameters in the termination phase of high confinement H-modes at JET and implications for ITER, Nuclear Fusion **54** (2014) 123014
- [14] Angioni C, Mantica P, Pütterich T et al, Tungsten transport in JET H-mode plasmas in hybrid scenario, experimental observations and modelling, Nuclear Fusion **54** (2014) 083028
- [15] Odstrcil T, Pütterich T, Angioni C et al, The physics of W transport illuminated by recent progress in W density diagnostics at ASDEX Upgrade, Plasma Physics and Controlled Fusion **60** (2018) 014003
- [16] Loarte A, Lipschultz B, Kukushkin A S et al, Chapter 4: Power and particle control, Nuclear Fusion 47 (2007) S203-S63